ACS OMEGA

http://pubs.acs.org/journal/acsodf

Article

Stepping toward Portable Optoelectronics with SnO_2 Quantum Dot-Based Electron Transport Layers

Muhammad Salman Kiani, Hryhorii P. Parkhomenko, Mayuribala Mangrulkar, Sabina Aigarayeva, Assylan Akhanuly, Erik O. Shalenov, Annie Ng, and Askhat N. Jumabekov*

Cite This: *ACS Omega* 2023, 8, 21212−21222

Read Online

ACCESS | Metrics & More | Article Recommendations | Supporting Information

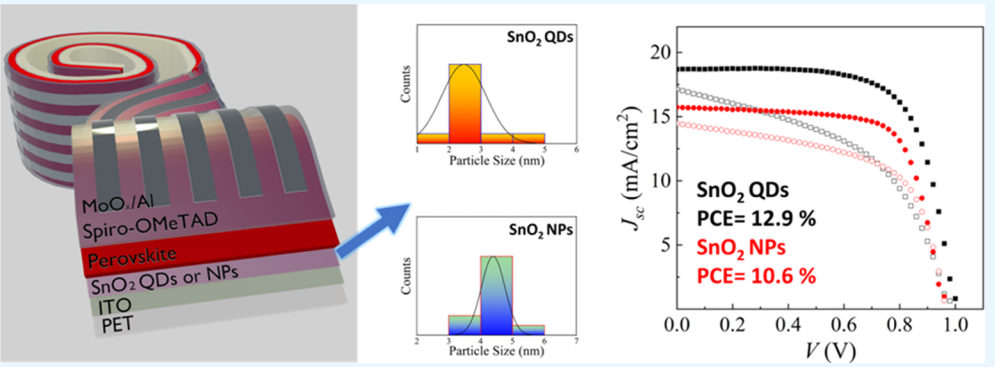

ABSTRACT: With a power conversion efficiency (PCE) of more than 25%, perovskite solar cells (PSCs) have shown an immense potential application for solar energy conversion. Owing to lower manufacturing costs and facile processibility via printing techniques, PSCs can easily be scaled up to an industrial scale. The device performance of printed PSCs has been improving steadily with the development and optimization of the printing process for the device functional layers. Various kinds of SnO_2 nanoparticle (NP) dispersion solutions including commercial ones are used to print the electron transport layer (ETL) of printed PSCs, and high processing temperatures are often required to obtain ETLs with optimum quality. This, however, limits the application of SnO_2 ETLs in printed and flexible PSCs. In this work, the use of an alternative SnO_2 dispersion solution based on SnO_2 quantum dots (QDs) to fabricate ETLs of printed PSCs on flexible substrates is reported. A comparative analysis of the performance and properties of the obtained devices with the devices fabricated employing ETLs made with a commercial SnO_2 NP dispersion solution is carried out. The ETLs made with SnO_2 QDs are shown to improve the performance of devices by ∼11% on average compared to the ETLs made with SnO_2 NPs. It is found that employing SnO_2 QDs can reduce trap states in the perovskite layer and improve charge extraction in devices.

INTRODUCTION

Organic−inorganic perovskites (OIPs) have attracted enormous attention in photovoltaics (PV) research due to their excellent optoelectronic properties (e.g., optimal band gap, low exciton binding energy, long charge carrier diffusion length, and low density of sub-band gap trap states), solution processability, and low cost.[1,2] Perovskite solar cells (PSCs) based on OIP photoactive layers have achieved a certified PCE of 25.7% in a matter of a decade.[3] Currently, PSCs are considered to be one of the fastest developing technology in PV research and are forecasted to make several viable commercial applications in emerging new technologies such as smart buildings, wearable and portable optoelectronics, the IoT technology, and the automobile industry.[4−7]

In a typical n−i−p-structured PSC, an OIP layer (layer with i-type conductivity) is sandwiched between an electron transport layer (ETL, layer with n-type conductivity) and a hole transport layer (HTL, layer with p-type conductivity).[8,9] The primary function of the ETL is to extract electrons from the OIP layer and efficiently transport them to the front contact.[10] The front contact is usually made of a transparent conducting oxide (TCO) such as fluorine- or indium-doped SnO_2 (FTO or ITO). The HTL, on the other hand, serves to block the flow of electrons while allowing holes to flow from the OIP layer to the back contact.[11] The most efficient PSCs to date are fabricated using the spin-coating technique. However, the spin-coating technique is not suitable for scale-up manufacturing of PSCs.[12,13] Inkjet printing, screen printing,

Received: April 7, 2023
Accepted: April 25, 2023
Published: June 1, 2023

slot-die coating, and blade coating, on the other hand, are some of the techniques that are more suitable for scale-up manufacturing of PSCs.[14,15] Among them, slot-die coating is one of the more appealing scalable printing techniques as it provides fast and effective deposition of solution-processed thin films on large areas with little material waste. In addition, this technique can be integrated into both roll-to-roll (R2R) and sheet-to-sheet (S2S) printing systems, which enables the fabrication of PSCs on both rigid and flexible substrates.[16,17]

Printed and flexible PSCs are of paramount importance for the industrialization of this technology and their successful application in other fields.[18,19] In these devices, flexible plastic substrates such as poly(ethylene terephthalate) (PET) or poly(ethylene naphthalate) (PEN) are used to deposit the device functional layers.[20,21] The use of plastic substrates, however, requires deposition and annealing of all device functional layers below 150 °C. Above this temperature, the required mechanical properties of plastic substrates alter or/and degrade, affecting the structural integrity of the device functional layers on top and deteriorating the overall PV performance of devices. Typically, the processing temperatures for HTLs and OIPs are less than 150 °C. However, higher processing temperatures are often required to obtain high-quality ETLs.[22−24] Hence, the fabrication of ETLs of PSCs on flexible substrates using printing techniques still requires further investigation and development.[25,26]

In n−i−p-structured PSCs, it is important to choose ETL materials with high optical transparency (in the visible range), high electron mobility, appropriate conduction and valence band energies, and low fabrication cost. SnO_2 is frequently used as an effective ETL material for PSCs due to its wide optical band gap (3.6−4.0 eV), deep conduction band, better transparency, high electron mobility (240 $cm^2\ V^{-1}\ s^{-1}$), long charge carrier diffusion length, and exceptional chemical stability.[27,28] However, processing of SnO_2 ETLs for PSCs may require temperatures above 180 °C.[29,30] Most reported printed and flexible PSCs employ commercially available SnO_2 NP dispersion solutions to prepare ETL inks and to fabricate ETLs of devices. However, the performance of resulting devices is still inferior to those fabricated on glass/TCO substrates and with SnO_2 ETLs processed at high temperatures.[31,32] Recently, ETL inks based on SnO_2 QD dispersion solutions have been used to manufacture efficient printed and flexible PSCs with SnO_2 ETLs deposited at lower temperatures.[33] Hence, this report aims to investigate the performance and device properties of printed flexible PSCs with SnO_2 QD-based ETLs and compare them with similarly made devices employing commercially available SnO_2 NP-based ETLs. The devices are manufactured using the slot-die coating technique employing thin PET films with a TCO layer as flexible substrates. The performance analysis and investigation of device properties are carried out employing both experimental and theoretical methods. The obtained results provide a valuable understanding of the effect of SnO_2 QD- and SnO_2 NP-based ETLs on the behavior and performance of devices.

EXPERIMENTAL SECTION

Materials. SnO_2 NP colloid dispersion (15 wt % colloidal dispersion in H_2O) is purchased from Alfa Aesar. Methylammonium iodide (MAI, 99.995%) is purchased from GreatCell Solar. Tin chloride dihydrate ($SnCl_2{\cdot}2H_2O$, 98%), lead iodide (PbI_2, 99%), 4-*tert*-butylpyridine (4tBp, 98%), chlorobenzene (CB, 99.80%), bis(trifluoromethane)-sulfonimide lithium salt (Li-TFSI, 99%), methylamine solution (MA, 33 wt % in absolute ethanol), acetonitrile (ACN, 99.80%), and acetone (99.80%) are purchased from Merck. 2,2′,7,7′-Tetrakis-(*N*,*N*-di-4-methoxyphenylamino)-9,9′-spirobifluorene (Spiro-MeOTAD, 99.50%) and (6,6)-phenyl C71 butyric acid methyl ester ($PC_{71}BM$) are purchased from Lumtec. Potassium hydroxide pellets (KOH, 85%) are purchased from ACS reagent. 2-Propanol (IPA, 99.80%) and ethanol (96.3%) are purchased from a local supplier. MoO_x, Al, and Ag are purchased from Kurt. J. Lesker. Patterned PET/ITO substrates (48 Ω sq^{-1}) are purchased from Mekoprint. All of the chemicals are used as received.

Ink Preparations. The ETL inks are prepared using as-synthesized SnO_2 QDs and commercial SnO_2 NP colloidal dispersion solution. SnO_2 QDs are synthesized using a previously reported solvothermal technique and have an average size of ∼2.5 nm.[33] The SnO_2 QD-based inks are obtained by dispersing SnO_2 QDs in an aqueous medium at a 2.0 wt % concentration.[33] To prepare the SnO_2 NP-based inks, a commercial SnO_2 NP dispersion solution is further diluted with water to obtain aqueous colloidal dispersions with a 2 wt % concentration of SnO_2 NPs. The obtained colloidal solutions (ETL inks) are then filtered using 0.45-μm-sized PTFE filters. For the preparation of the perovskite (methylammonium lead iodide, $MAPbI_3$) inks, PbI_2 and MAI are used as precursors, while MA and ACN are used as solvents. Preparation of the perovskite ink involves dissolving 1 mol of PbI_2 and MAI each in 700 μL of MA. The solution is stirred at 70 °C and 460 rpm for an hour using a hot plate and a magnetic stirrer. Next, 700 μL of ACN is added to the solution and stirred at 460 rpm at room temperature for an additional 3 h. A 0.45-μm-sized PTFE filter is then used to filter the perovskite ink. The HTL ink is prepared simply by dissolving 45 mg of Spiro-MeOTAD in 1 mL of CB using a vortex shaker. After 1 h of shaking at 460 rpm, 28.8 μL 4tBp and 17.5 μL lithium salt solution (520 mg mL^{-1} of Li-TFSI in ACN) are added to Spiro-MeOTAD/CB solution as additives. A 0.45-μm-sized PTFE filter is then used to filter the HTL ink. For the fabrication of electron-only devices, a $PC_{71}BM$ solution in CB is prepared by dissolving 10 mg of $PC_{71}BM$ in 1 mL of CB. The solution is stirred at 90 °C and 460 rpm for an hour using a hot plate and a magnetic stirrer. The final solution is then filtered using a 0.45-μm-sized PTFE filter.

Substrate Preparation. PET/ITO substrates are used to fabricate printed and flexible PSCs. For this, the PET/ITO substrates are cleaned by washing them for 10 min in DI water with a detergent, clean DI water, acetone, and IPA while sonicating them using an ultrasonic bath. After drying them under a stream of compressed air, the substrates are treated with ultraviolet−ozone (UV−ozone) for 15 min.

Device Fabrication. A slot-die coater with a slot-die head (FOM Technologies, Denmark) is used to print main device functional layers (ETL, perovskite, and HTL). All device functional layers are printed in an ambient atmosphere at 25 °C and relative humidity of 40−60%. To fabricate devices, ETLs are printed on PET/ITO substrates. For this, freshly prepared SnO_2 QD-based inks are slot-die-coated on clean PET/ITO substrates and annealed at 140 °C for 30 min using a vacuum hot plate. Then, freshly prepared perovskite inks are printed on top of ETLs and the substrates are annealed at 100 °C for 10 min. Next, HTL inks are printed on top of the perovskite layer. The temperature of the slot-die coater

https://doi.org/10.1021/acsomega.3c02341
ACS Omega 2023, 8, 21212−21222

substrate chuck is kept at 25 °C during all printing steps. Exactly the same protocol is used to print devices with SnO_2 NP-based ETLs. After the deposition of all functional layers, the substrates are stored in a dry box overnight to improve the hole-transporting properties of Spiro-MeOTAD HTLs. Finally, MoO_x/Al contacts are deposited on top of HTLs using a thermal evaporator (Nexdep PVD, Angstrom, Canada). A schematic sketch of the structure and band diagram[34] of the fabricated devices are presented in Figure 1a,b, respectively.

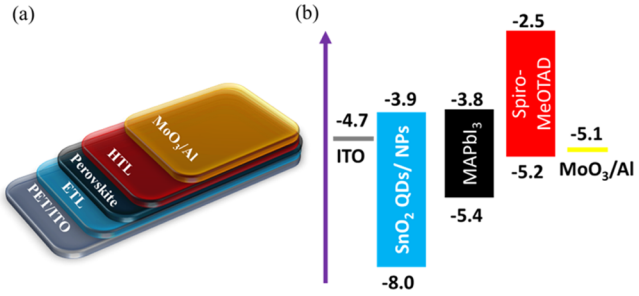

Figure 1. Schematic diagram of the (a) structure of printed and flexible PSCs and (b) the device band diagram.

Table S1 (see the Supporting Information) displays the coating parameters used for slot-die coating of the functional layers of devices. For the fabrication of electron-only devices, a $PC_{71}BM$/CB ink is slot-die-coated on top of the perovskite layer instead of HTL and Ag contacts are deposited on top using the thermal evaporator.

Device Characterization. A transmission electron microscope (TEM, JEOL JEM-1400 Plus, Japan) is used to estimate the crystallinity and particle size of SnO_2 QDs and SnO_2 NPs. An X-ray diffractometer (XRD, SmartLab Rigaku) is used to examine the crystal structure of SnO_2 QDs and SnO_2 NPs (using Cu Kα = 1.5418 Å). A scanning electron microscope (SEM, Zeiss Crossbeam 540, Germany) is used to obtain cross-sectional-view SEM micrographs of devices with SnO_2 QD- and SnO_2 NP-based ETLs. For better cross-sectional SEM imaging and analysis of the thickness of the functional layers, devices are fabricated on glass instead of PET/ITO substrates. Top-view SEM micrographs of SnO_2 QD- and SnO_2 NP-based ETLs are also recorded to study their morphology. Light transmittance of SnO_2 QD- and SnO_2 NP-based ETLs on glass substrates is measured using a UV−visible (UV−vis) spectrometer (Lambda 1050, PerkinElmer). The elemental composition of SnO_2 QD- and SnO_2 NP-based ETLs on ITO glass substrates is determined using an X-ray photoelectron spectroscope (XPS, Nexsa, Thermo Scientific). Device performance is characterized using a solar simulator (Oriel Sol3A, Newport) and a Keithley 2400 source measure unit (Keithley). Current density−voltage (J−V) curves of devices are recorded at a scan rate of 400 mV s^{-1} between −0.2 V and +1.2 V. The fabricated devices have an active area of 0.1 cm^2, and a mask with an active area of 0.03 cm^2 is used to plot their J−V curves. An FLS 1000 spectrometer (Edinburgh Instruments, U.K.) is used to perform photoluminescence (PL) studies. Open-circuit voltage decay (OCVD) curves of devices are measured using a potentiostat/galvanostat instrument (Autolab PGSTAT302N, Metrohm, Switzerland). An external quantum efficiency (EQE) measurement system (ORIEL IQE-200) is used to record the EQE spectra of devices.

Computer Simulation and Modeling. COMSOL Multiphysics software is used for computer simulation and modeling experiments. The wavelength dependence of refractive index n, extinction coefficient k, and real part of complex permittivity ε of the materials employed in the optical simulation experiments are taken from the literature (see Figure S1 of the Supporting Information).[35,36] Theoretical J−V curves of devices are obtained using the standard drift-diffusion model. More details about the computer simulation and modeling method employed in this work can be found in our previous reports.[35,37,38]

RESULTS AND DISCUSSION

The TEM is used to estimate and compare the particle sizes of SnO_2 QDs and SnO_2 NPs employed in the experiments. For

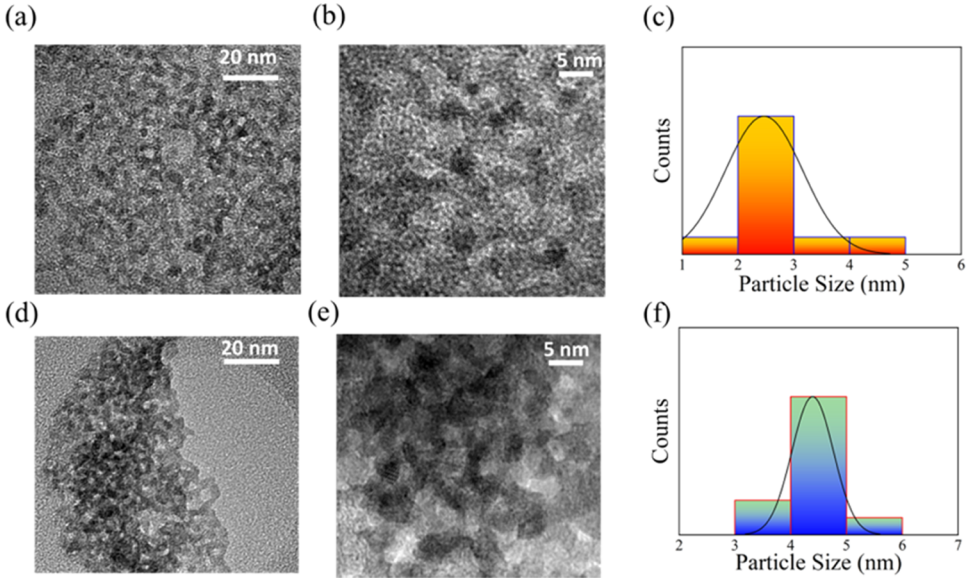

Figure 2. TEM micrographs of SnO_2 QDs obtained at (a) lower and (b) higher magnification. (c) Particle size distribution curve for SnO_2 QDs. TEM micrographs of SnO_2 NPs obtained at (d) lower and (e) higher magnification. (f) Particle size distribution of SnO_2 NPs.

https://doi.org/10.1021/acsomega.3c02341
ACS Omega 2023, 8, 21212−21222

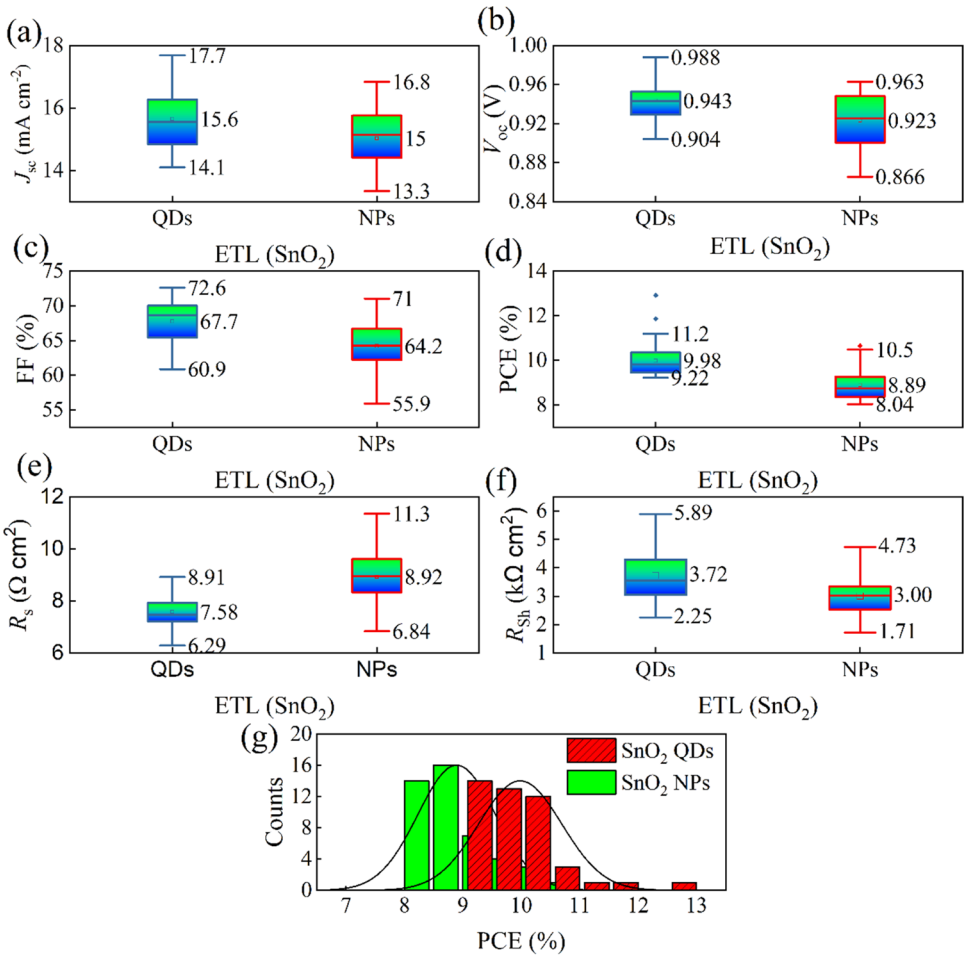

Figure 3. Comparison of (a) J_{sc}, (b) V_{oc}, (c) FF, (d) PCE, (e) R_s, and (f) R_{Sh} of the experimentally obtained PSCs with SnO_2 QD- and SnO_2 NP-based ETLs. (g) Comparison of PCE distribution in the devices with SnO_2 QD- and SnO_2 NP-based ETLs.

this, TEM micrographs are obtained for the samples with SnO_2 QDs (Figure 2a,b) and SnO_2 NPs (Figure 2d,e). Figure 2b,e indicates that the SnO_2 QDs and SnO_2 NPs are crystalline and have rather uniform size distributions. The estimated average particle size of SnO_2 QDs is around 2.5 nm (see Figure 2c), which is smaller than the Bohr exciton radius of SnO_2 (2.70 nm).[32] The average particle size of SnO_2 NPs is around 4.5 nm (see Figure 2f). The recorded X-ray diffractograms of the samples with SnO_2 QDs and SnO_2 NPs (see Supporting Information Figure S2) also show that the particles of SnO_2 QDs and SnO_2 NPs are crystalline.

To fabricate printed and flexible PSCs with ETLs made of SnO_2 QDs and SnO_2 NPs, the ETL inks based on SnO_2 QDs and SnO_2 NPs are slot-die-coated on top of clean PET/ITO substrates. A top-view SEM analysis is conducted on the ETL-coated PET/ITO substrates to investigate the surface coverage and uniformity of the obtained SnO_2 QD- and SnO_2 NP-based ETLs. The SEM micrographs (see Figure S3 in the Supporting Information) indicate that there are no discernible pinholes in the ETLs, which implies that both types of ETLs cover the surface of PET/ITO substrates rather uniformly. Next, the $MAPbI_3$ perovskite layer is slot-die-coated on top of freshly prepared SnO_2 QD- and SnO_2 NP-based ETLs on PET/ITO substrates. Once the perovskite layer is formed, a Spiro-MeOTAD-based HTL is slot-die-coated on top of the perovskite layer. The device fabrication process is completed by depositing MoO_x/Al contacts using a thermal evaporator. The cross-sectional-view SEM micrographs of the obtained devices are shown in Figure S4 (see Figure S4 in the Supporting Information).

The device performance of the obtained devices is investigated in ambient conditions without any encapsulation. Figure 3 displays a comparison of the solar cell parameters of the obtained devices. In total, 45 devices are analyzed for both types of ETLs. Here, the comparison is shown for short-circuit current density (J_{sc}), open-circuit voltage (V_{oc}), fill factor (FF), PCE, series resistance (R_s), and shunt resistance (R_{Sh}). The R_s and R_{Sh} are calculated using the differential resistance method (see Figure S5 in the Supporting Information for details). The average values of the solar cell parameters are displayed in Table S2 (see the Supporting Information).

Figure 3a,b indicates that the J_{sc} and V_{oc} values of the devices with SnO_2 QD-based ETLs are higher than those with SnO_2 NP-based ETLs. The devices with SnO_2 QD-based ETLs have higher average J_{sc}, V_{oc}, and FF values than in those with SnO_2 NP-based ETLs. Due to this, the average PCE of the devices with SnO_2 QD-based ETLs is higher by ∼11% than in those with SnO_2 NP-based ETLs. Figure 3e,f shows that SnO_2 QD-based ETLs offer lower R_s and higher R_{Sh} in devices than SnO_2 NP-based ETLs. This could be due to the more compact nature of SnO_2 QD-based ETLs compared to their SnO_2 NP-based alternative. Figure 3g depicts that the majority of devices with SnO_2 QD-based ETLs have PCE values around 9−10.5%, while it is 8−9% for the devices with SnO_2 NP-based ETLs.

https://doi.org/10.1021/acsomega.3c02341
ACS Omega 2023, 8, 21212−21222

Figure 4a shows the $J-V$ curves of the best-performing devices with SnO_2 QD- and SnO_2 NP-based ETLs. The solar

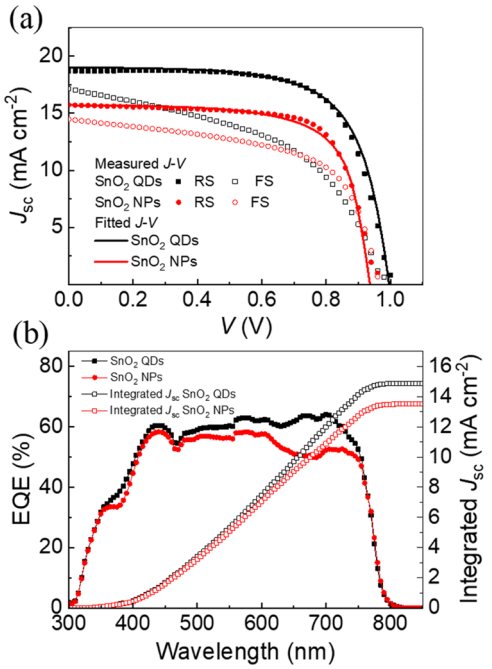

Figure 4. Comparison of (a) $J-V$ curves and (b) EQE spectra of champion devices with SnO_2 QD- and SnO_2 NP-based ETLs under AM1.5G condition.

cell parameters of these devices are presented in Table 1. A PCE value of around 12.91% is obtained for the best-performing device with SnO_2 QD-based ETLs. This is higher than the highest PCE (10.6%) obtained in devices with SnO_2 NP-based ETLs by ∼18%. The $J-V$ curves of the devices show a considerable hysteresis. This could be due to the fabrication of the devices in an ambient environment with relatively high humidity (40−60%) and without the use of passivation strategies to improve the ETL/perovskite interface. Furthermore, the spectral responses of these devices are also evaluated by comparing their recorded EQE spectra (see Figure 4b). The EQE spectra of the devices are typical for $MAPbI_3$-based devices and well above 50% over the visible spectrum.[39,40] The device with SnO_2 QD-based ETLs shows higher EQE values throughout the measurement range compared to the device with SnO_2 NP-based ETLs. Here, a significant gain in the EQE values of the former is in the 600−750 nm wavelength range, which is up to ∼15% higher than the EQE values of the latter device for the same wavelengths. The J_{sc} values obtained from the integration of the EQE spectra yield 15 and 13.5 mA cm^{-2} for the device with SnO_2 QD- and SnO_2 NP-based ETLs (See Table 1), respectively. This is qualitatively consistent with the J_{sc} values obtained from the $J-V$ measurements (see Figure 4a and Table 1).

The above findings indicate that the devices with SnO_2 QD-based ETLs, in general, perform better than those with SnO_2 NP-based ETLs. The main difference between these two types of ETLs is in the sizes of SnO_2 particles. It is possible that this can influence the interface between the ETL and perovskite layers. Different sizes of SnO_2 particles may result in a difference in the optical properties of its ETLs, which, subsequently, can influence carrier generation in the perovskite layer and also can influence the carrier extraction and recombination process at the ETL/perovskite interface.[41−43] However, the UV−vis transmittance measurements performed on SnO_2 QD- and SnO_2 NP-based ETLs on glass (see Figure S6 in the Supporting Information) show that these two types of ETLs have a comparable optical transparency. This means that, roughly, the same amount of light is transmitted to the perovskite layer upon illumination and the size difference between the SnO_2 QD and the SnO_2 NP is not the origin of the performance difference in the devices. If the perovskite layer in devices with these two different types of ETLs has the same thickness and structure, which is roughly the case in the obtained devices, carrier generation in the perovskite layer under the same light illumination can also be assumed the same. Hence, the origin of the discrepancy in the performance between the devices with the SnO_2 QD- and SnO_2 NP-based ETLs is not the difference in carrier generation but possibly due to carrier extraction and recombination processes at the ETL/perovskite interfaces.

The extraction coefficient that characterizes the charge carrier extraction processes, approximately, can be defined by the following relation

$$c_{ex}(V) \approx \frac{J_{sc}}{J_{gen}} \tag{1}$$

where J_{gen} is the current density of photogenerated charge carriers and J_{sc} is short-circuit current density.[44] The current of photogenerated carriers in solar cells includes two components: current density due to holes (J_p) and electrons (J_n). J_{gen} is described by the following equations[38,43]

$$J_{gen} = J_p + J_n \tag{2}$$

where,

$$J_p = qn\mu_p E_v + \mu_p k_B T \nabla p \tag{3}$$

$$J_n = qn\mu_n E_c + \mu_n k_B T \nabla n \tag{4}$$

Here, $E_v = -\nabla(V + \chi_0 + E_{g,0})$ and $E_c = -\nabla(V + \chi_0)$ are the valence and conduction band energies, respectively, $E_{g,0}$ is the

Table 1. Solar Cell Performance Parameters of Champion Devices with SnO_2 QD- and SnO_2 NP-Based ETLs under AM1.5G Condition

ETL	scan direction	J_{sc} (mA cm^{-2})	V_{oc} (V)	FF (%)	PCE (%)	R_s (Ω cm^2)	R_{sh} (kΩ cm^2)	integrated J_{sc} (mA cm^{-2})
SnO_2 QDs	reverse	18.8	0.99	69	12.9	3.86	1.01	
	theoretical	19.0	1.00	68	12.9	3.8	1.01	15.0
	forward	17.3	0.97	48	8.1	3.98	0.17	
SnO_2 NPs	reverse	15.73	0.956	71	10.6	3.97	0.91	
	theoretical	15.7	0.94	69	10.3	3.96	0.92	13.5
	forward	14.47	0.965	59	8.2	4.68	0.32	

https://doi.org/10.1021/acsomega.3c02341
ACS Omega 2023, 8, 21212−21222

band gap, χ_0 is the electron affinity, μ_n is the mobility of electrons, and μ_p is the mobility of holes. Since the hole selective layer is the same in the fabricated devices with SnO_2 QD- and SnO_2 NP-based ETLs, the current generated by the holes can be considered the same. In this case, the difference in charge carrier extraction is determined by J_n.

To better understand charge transfer between the perovskite layer and SnO_2 QD- and SnO_2 NP-based ETLs, steady-state PL measurements are conducted for a neat perovskite film on the glass as well as for the SnO_2 QD-based ETL/perovskite and SnO_2 NP-based ETL/perovskite films on glass. Figure 5

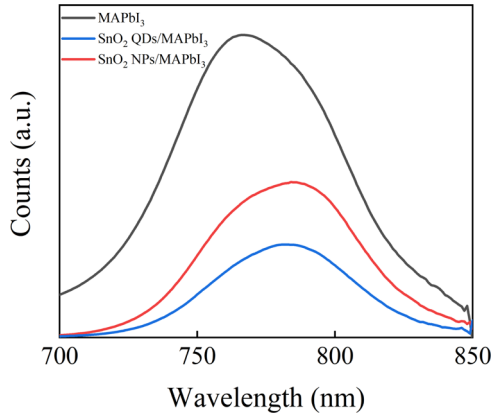

Figure 5. Comparison of the steady-state PL spectra of neat perovskite, SnO_2 QD-based ETL/perovskite, and SnO_2 NP-based ETL/perovskite films on glass.

shows that the neat perovskite film has a PL peak at around 775 nm, which is typical for $MAPbI_3$. The PL peak of the SnO_2 QD-based ETL/perovskite film and the SnO_2 NP-based ETL/perovskite film is considerably lower than the PL peak of the neat perovskite film, i.e., SnO_2 ETLs partially quench the PL emission of the perovskite layer. This indicates the occurrence of charge transfer from the perovskite layer to SnO_2 ETLs. Figure 5 also depicts that the PL peak of the SnO_2 NP-based ETL/perovskite film is considerably higher than that of the SnO_2 QD-based ETL/perovskite film. This suggests that charge extraction by SnO_2 QD-based ETLs is more effective than it is in SnO_2 NP-based ETLs. These findings clearly point to a certain difference in the properties of the ETL/perovskite interface for SnO_2 QD- and SnO_2 NP-based ETLs. Hence, investigation of the physical properties of this interface may give some insights into the observed performance difference in the devices with SnO_2 QD- and SnO_2 NP-based ETLs.

Space-charge-limited current (SCLC) measurements carried out with electron- or hole-only devices are useful for determining charge carrier mobility and density of trap states in semiconductors.[45−47] Thus, fabricating electron-only devices with SnO_2 QD- and SnO_2 NP-based ETLs can provide some insights into how different ETLs affect these parameters in the perovskite layer and help to probe the properties of the ETL/perovskite interface in devices. With this in mind, electron-only devices are printed using SnO_2 QD- and SnO_2 NP-based ETLs and the $J-V$ characteristics of the obtained devices are investigated. Figure 6 shows the $J-V$ characteristics of the electron-only devices, and the inset graph depicts the structure of prepared electron-only devices. The $J-V$ curves of the electron-only devices display three distinct regions. The first region is at low voltages with a slope of 1. The second is at

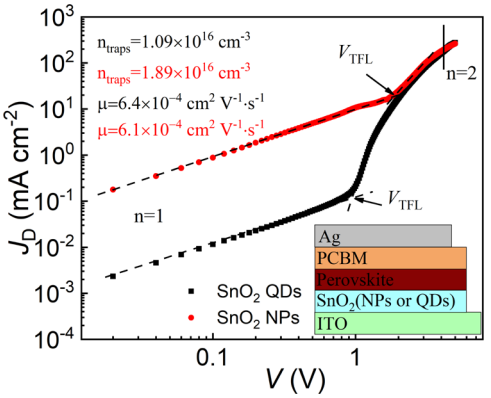

Figure 6. Comparison of $J-V$ curves of electron-only devices with SnO_2 QD- and SnO_2 NP-based ETLs.

intermediate voltages with a slope of 2. This region is referred to as the trap-filling regime.[45,46] Finally, the third region, which is referred to as the SCLC region with a slope of more than 2, appears at high voltages.[45] The electron mobility from the SCLC region is estimated using the Mott−Gurney equation

$$\mu_n = \frac{8J_D A^3}{9\varepsilon\varepsilon_0 V^2} \quad (5)$$

where J_D is the current density, V is the applied voltage, ε (equal to 28.8) is the relative dielectric constant of $MAPbI_3$ perovskite,[47,48] ε_0 is the vacuum permittivity, and A (equal to 550 nm) is the thickness of the $MAPbI_3$ film.

The estimated μ_n values in the perovskite layer of the electron-only devices with SnO_2 QD- and SnO_2 NP-based ETLs are 6.4×10^{-4} and 6.1×10^{-4} cm^2 V^{-1} s^{-1}, respectively. Here, μ_n for the device with SnO_2 QD-based ETLs is slightly higher than the value of μ_n obtained for the device with SnO_2 NP-based ETLs. While this might be in favor of SnO_2 QD-based ETLs, this small difference in the μ_n values, however, is not large enough to produce the notable difference observed in the J_{sc} values of the fabricated devices (see Figures 3a and 4a). Hence, the origin of the difference in the carrier extraction coefficient in devices with SnO_2 QD- and SnO_2 NP-based ETLs might be related to the concentration of charge carriers, which, in turn, is a function of the recombination processes taking place in devices.[43]

In general, carrier recombination in PSCs includes three main components: radiative, Shockley−Read−Hall (SRH), and surface recombination. Radiative recombination in the perovskite layer is a characteristic of the material and should not change depending on the carrier selective layers. Hence, the difference in carrier recombination in the devices with SnO_2 QD- and SnO_2 NP-based ETLs is mainly due to the SRH and surface recombination processes. To quantify the recombination processes in the devices, the values for the density of trap states are calculated using the following relation

$$n_{trap} = \frac{2\varepsilon\varepsilon_0 V_{TFL}}{(qA^2)} \quad (6)$$

where q is the elementary charge and V_{TFL} is the trap-filled-limit voltage estimated from SCLC measurements with the electron-only devices.[49,50] The estimated value of n_{trap} in the perovskite layer of the device with SnO_2 QD-based ETLs is 1.16×10^{16} cm^3, whereas it is 1.89×10^{16} cm^3 in the device with SnO_2 NP-based ETLs. These results show that the use of

https://doi.org/10.1021/acsomega.3c02341
ACS Omega 2023, 8, 21212−21222

SnO_2 NPs to form ETLs results in more trap states in the perovskite layer.

To gain a further understanding of the recombination processes, the dependence of V_{oc} and J_{sc} on light intensity in the obtained PSCs is investigated.[51−53] For this, the $J-V$ curves of the best-performing PSCs with SnO_2 QD- and SnO_2 NP-based ETLs (see Figure 4a) are measured under different light intensities using neutral density filters (see Figure S7 in the Supporting Information). The dependence of J_{sc} on the light intensity appears linear (see the inset graph in Figure 7) for both devices. This indicates that recombination losses in the devices under the short-circuit condition are small.[54]

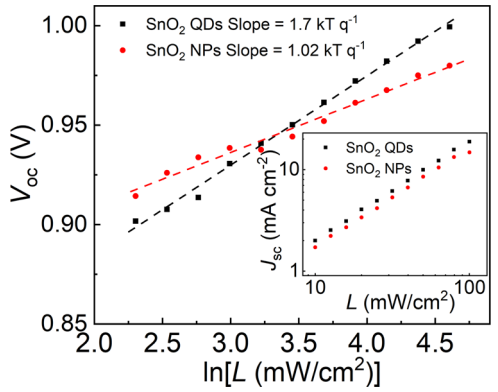

Figure 7. Comparison of the dependence of V_{oc} and J_{sc} of the best-performing PSCs with SnO_2 QD- and SnO_2 NP-based ETLs on light intensity.

The dependence of V_{oc} vs light intensity can be described by the following equation[38,55,56]

$$V_{oc} = \frac{n_{idL} k_B T \ln(L)}{q} \quad (7)$$

where n_{idL} is the light ideality factor, T is the absolute temperature, k_B is Boltzmann's constant, and L is the light intensity. It is possible to determine n_{idL} from the slope of the dependence of V_{oc} on $\ln(L)$. The estimated value of n_{idL} from Figure 7 for the device with SnO_2 QD-based ETLs is around 1.7. This indicates that the dominant recombination in this device is due to SRH recombination.[54,55,57] The dominance of SRH recombination in PSCs is usually attributed to the defects within the perovskite active layer.[58,59] As for the device with SnO_2 NP-based ETLs, the estimated value of n_{idL} is 1.02. This is considerably lower than the n_{idL} value in the device with SnO_2 QD-based ETLs. The decrease in n_{idL} is usually attributed to the surface recombination effects.[60,61] Based on this, it can be suggested that, in addition to the SRH recombination, there is a considerable loss of photogenerated charge carriers due to surface recombination in the devices with SnO_2 NP-based ETLs. This is further supported by open-circuit voltage decay (OCVD) measurements performed with the devices, which show higher electron lifetime (τ) values (around maximum power point and lower voltages) in the device with SnO_2 QD-based ETLs compared to the device with SnO_2 NP-based ETLs (see Figure S8 in the Supporting Information).

To further understand the experimentally obtained results, the $J-V$ curves (reverse scans) of the best-performing devices with SnO_2 QD- and SnO_2 NP-based ETLs are modeled using numerical simulation methods. For this, the experimentally determined perovskite layer electronic parameters such as charge carrier mobility (estimated from SCLC measurements, see Figure 6) and electron lifetime (estimated from OCVD measurements, see Figure S8 in the Supporting Information) as well as the literature values of material parameters of the device functional layers (see Table S3 in the Supporting Information) are used to obtain the theoretical $J-V$ curves (see Figure 4a and Table 1) that closely match the experimental ones. The simulation experiments show that

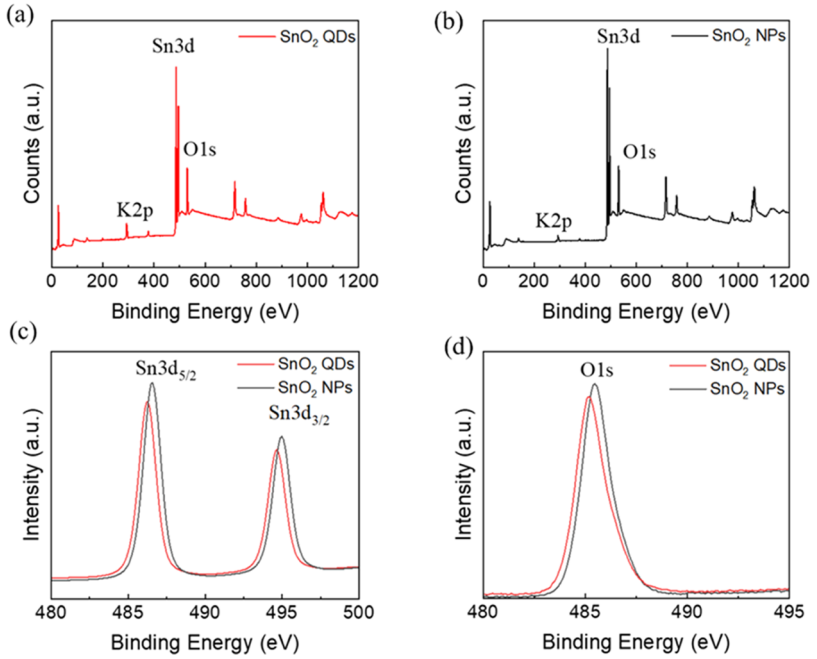

Figure 8. XPS spectra of (a) SnO_2 QD- and (b) SnO_2 NP-based ETLs. Comparison of the magnified XPS spectra of SnO_2 QD- and SnO_2 NP-based ETLs for (c) Sn and (d) O peaks, respectively.

https://doi.org/10.1021/acsomega.3c02341
ACS Omega 2023, 8, 21212−21222

surface recombination speed is higher in the device with SnO_2 NP-based ETLs than it is in the device with SnO_2 QD-based ETLs. This indicates that charge carrier recombination at the ETL/perovskite interface in the device with SnO_2 NP-based ETLs is also higher, and this could be due to high concentration of surface defects at this interface. This is consistent with the above-presented experimental studies.

A higher degree of charge extraction at the SnO_2 QD-based ETL/perovskite interface in devices might be correlated with lower oxygen vacancies in SnO_2 QDs compared to SnO_2 NPs. Lower oxygen vacancies in SnO_2 imply a lower concentration of trap states in its ETLs and better device performance.[62−64] To investigate this, XPS analysis is performed on SnO_2 QD- and SnO_2 NP-based ETLs on glass. The XPS spectra recorded for the samples are shown in Figure 8, in which Figure 8a,b shows the entire XPS spectra of the samples, whereas Figure 8c,d shows the magnified images of the spectral peaks associated with tin (Sn) and oxygen (O). Figure 8a,b also shows the presence of potassium (K) impurities in the samples. Potassium originates from the potassium hydroxide additive in the ETL inks, which is used to stabilize the SnO_2 QD and SnO_2 NP colloidal solutions.[15] Table 2 shows the elemental ratio of Sn, O, and K in SnO_2 QD- and SnO_2 NP-based ETLs obtained from Sn 3d, O 1s, and K 2p XPS peaks. The ratio of O 1s to Sn 3d for SnO_2 QD- and SnO_2 NP-based ETLs yields values of 3.72 and 3.48, respectively, indicating lower oxygen vacancies in the former. Additionally, the elemental ratio of K in SnO_2 QD-based ETLs appears more than 2 times higher than that in SnO_2 NP-based ETLs. It is noteworthy to mention that potassium ions can act as an effective passivating agent for the perovskite layer surface defects.[65−67] Hence, it is reasonable to suggest that the improved performance of printed and flexible PSCs with SnO_2 QD-based ETLs compared to their SnO_2 NP-based alternative could indeed be due to a lower concentration of oxygen vacancies in the former. Additionally, a higher concentration of the potassium ions sitting on the surface of SnO_2 QD-based ETLs helps to better passivate the surface defects of the perovskite layer at the ETL/perovskite interface. This, in turn, affords reduced density of trap states and hindered surface recombination. Overall, based on above findings, it is apparent that the particles of SnO_2 forming ETLs should not have many defects in the form of oxygen vacancies to result in more ideal surface to extract charges from the perovskite layer. This could be achieved by further optimizing the synthesis protocol for the preparation of SnO_2 QDs or NPs and employing various passivating strategies using inorganic or organic passivating agents.[34] Moreover, the formation of the perovskite layer on more defect-free ETL surfaces can yield films with improved crystallinity and reduced surface defects, which would decrease surface recombination losses and provide a higher J_{SC} and V_{oc} in devices. Additionally, an improved ETL/perovskite interface can also help to reduce the hysteresis effect, which is a necessary condition to obtain devices with stable operation.

Table 2. XPS Elemental Ratio of Sn, O, and K in SnO_2 QD- and SnO_2 NP-Based ETLs

	atomic percentage	
element	SnO_2 QDs	SnO_2 NPs
Sn 3d	18.72	21.29
O 1s	69.68	74.17
Sn 3d/O 1s	3.72	3.48
K 2p	11.6	4.54

Finally, the mechanical stability of the devices with SnO_2 QD- and SnO_2 NP-based ETLs are investigated by performing bending tests. The solar cell parameters of the devices are estimated after the application of bending cycles. Here, a bending cycle involved repeated bending of devices 10 times to a curvature with a radius of 1 cm. Overall, the photovoltaic parameters of the devices with SnO_2 QD- and SnO_2 NP-based ETLs show rather similar trends with the applied bending cycles (see Figure S9 in the Supporting Information). In the initial stages of bending cycles, the V_{oc} of the device with SnO_2 NP-based ETLs appears to degrade slightly faster compared to the device with SnO_2 QD-based ETLs (see Figure S9b in the Supporting Information). This could be associated with the appearance of a slightly larger number of cracks and defects in the perovskite layer of the device with SnO_2 NP-based ETLs, which would lead to increased recombination losses of charge carriers and lower V_{oc}. Overall, the PCE values of the devices drop by around 75% of their initial values after the first bending cycle and become almost negligible after the second bending cycle (see Figure S9d in the Supporting Information). The observed degradation of the photovoltaic parameters of the devices during the bending test can be mainly attributed to the deteriorations (cracking) in the ITO layer, which leads to significant increases in the series resistance values of devices and strongly affects device current and FF.[68−70] This can be improved by employing alternative materials to TCOs that are more durable and resilient[71] or also can be mitigated by using various interlayers that can enhance the mechanical stability of the TCO layers.[72−74]

CONCLUSIONS

In summary, the fabrication of slot-die-printed flexible PSCs with SnO_2 QD- and SnO_2 NP-based ETLs is carried out and the effect of these ETLs on the overall device performance is investigated. On average, the devices with SnO_2 QD-based ETLs are shown to perform better than the devices with SnO_2 NP-based ETLs. A champion device with a PCE of 12.91% is obtained using SnO_2 QD-based ETLs, whereas the best-performing devices with SnO_2 NP-based ETLs have shown a PCE of around 10.6%. The PL measurements with ETL/perovskite samples showed a better quenching of PL emission in the perovskite layer with SnO_2 QD-based ETLs than with SnO_2 NP-based ETLs. The experiments with electron-only devices revealed that the perovskite layer of devices with SnO_2 QD-based ETLs have higher electron mobility values and lower trap states than in devices with SnO_2 NP-based ETLs. Additionally, V_{oc} vs light intensity and the OCVD measurements performed on the obtained PSCs showed that the devices with SnO_2 QD-based ETLs have lower recombination losses compared to the devices with SnO_2 NP-based ETLs. This is also supported by numerical simulation experiments, which also revealed lower surface recombination in devices with SnO_2 QD-based ETLs. These findings indicate that a better performance of SnO_2 QD-based ETLs in the obtained PSCs could be due to a more favorable condition at the ETL/perovskite interface for the charge extraction process. An underlying reason for this might be due to the more optimal material electronic properties of SnO_2 QD-based ETLs, which may originate from lower oxygen vacancies and high concentrations of potassium ions in SnO_2 QDs as opposed to SnO_2 NPs. The findings of this work demonstrate that the

https://doi.org/10.1021/acsomega.3c02341
ACS Omega 2023, 8, 21212−21222

use of SnO_2 QDs to prepare ETLs for printed and flexible PSCs can be a promising alternative to commercially available SnO_2 NPs in terms of fabricating efficient devices at moderate temperatures and could be useful in paving the way for developing more industrially friendly manufacturing methods.

■ ASSOCIATED CONTENT

Supporting Information

The Supporting Information is available free of charge at https://pubs.acs.org/doi/10.1021/acsomega.3c02341.

Coating parameters for functional layers printing via a vectorSC slot-die coater (Table S1); refractive index n and extinction coefficient k of PET, ITO, SnO_2 (ETL), $MAPbI_3$ (perovskite), and Spiro-MeOTAD (HTL) (Figure S1); XRD patterns of SnO_2 QDs and SnO_2 NPs (Figure S2); SEM top-view images (Figure S3); SEM cross-sectional images (Figure S4); statistical data for the photovoltaic parameters (Table S2); determination of the R_s and R_{sh} of devices using the differential resistance method (Figure S5); UV−vis transmittance spectra (Figure S6); $J-V$ curves of printed and flexible PSCs at different light intensity (Figure S7); OCVD curves for the devices (Figure S8); physical parameters used in numerical simulation experiments (Table S3); and comparison of the dependencies of (a) J_{sc}, (b) V_{oc}, (c) FF, and (d) PCE of devices with SnO_2 QD- and SnO_2 NP-based ETLs on the number of bending cycles (Figure S9) (PDF)

■ AUTHOR INFORMATION

Corresponding Author

Askhat N. Jumabekov − *Department of Physics, School of Sciences and Humanities, Nazarbayev University, Astana 010000, Kazakhstan;* orcid.org/0000-0003-0051-9542; Email: askhat.jumabekov@nu.edu.kz

Authors

Muhammad Salman Kiani − *Department of Physics, School of Sciences and Humanities, Nazarbayev University, Astana 010000, Kazakhstan*

Hryhorii P. Parkhomenko − *Department of Physics, School of Sciences and Humanities, Nazarbayev University, Astana 010000, Kazakhstan;* orcid.org/0000-0001-5358-1505

Mayuribala Mangrulkar − *Department of Physics, School of Sciences and Humanities, Nazarbayev University, Astana 010000, Kazakhstan*

Sabina Aigarayeva − *Department of Physics, School of Sciences and Humanities, Nazarbayev University, Astana 010000, Kazakhstan*

Assylan Akhanuly − *Department of Physics, School of Sciences and Humanities, Nazarbayev University, Astana 010000, Kazakhstan*

Erik O. Shalenov − *Department of General Physics, Satbayev University, Almaty 050013, Kazakhstan;* orcid.org/0000-0001-6469-6623

Annie Ng − *Department of Electrical and Computer Engineering, School of Engineering and Digital Sciences, Nazarbayev University, Astana 010000, Kazakhstan;* orcid.org/0000-0002-5975-2499

Complete contact information is available at: https://pubs.acs.org/10.1021/acsomega.3c02341

Author Contributions

M.S.K. performed the synthesis of SnO_2 QDs and fabrication of devices. M.S.K also performed TEM, SEM, XRD, XPS, UV−vis, PL, $J-V$, EQE, OCVD, and bending test measurements. H.P.P. contributed to the graphical abstract, $J-V$, EQE, and OCVD measurements and discussion. M.M. contributed to the PL measurements and discussion. S.A. contributed to the synthesis of SnO_2 QDs. A.A. and E.O.S. performed computer modeling experiments and discussion. The manuscript was mainly written by the first author M.S.K. and A.N.J. A.N. and A.N.J. designed research and supervised overall work. All authors discussed the results and commented on the manuscript.

Notes

The authors declare no competing financial interest.

■ ACKNOWLEDGMENTS

This work was supported by Research Grants from the Ministry of Science and Higher Education of the Republic of Kazakhstan (Grant Numbers: AP14869871 and AP14869983) and Nazarbayev University Collaborative Research Grant (Grant Number: 021220CRP1922). The authors thank the Core Facilities' team of Nazarbayev University for their help and support with the measurements.

■ REFERENCES

(1) Seo, J.; Noh, J. H.; Seok, S. I. Rational Strategies for Efficient Perovskite Solar Cells. *Acc. Chem. Res.* **2016**, *49*, 562−572.

(2) Oh, K.; Jung, K.; Shin, J.; Ko, S.; Lee, M.-J. Novel Intense-Pulsed-Light Synthesis of Amorphous SnO_2 Electron-Selective Layers for Efficient Planar $MAPbI_3$ Perovskite Solar Cells. *J. Mater. Sci. Technol.* **2021**, *92*, 171−177.

(3) Best Research-Cell Efficiency Chart. https://www.nrel.gov/pv/cell-efficiency.html. (accessed December 14, 2022).

(4) Kim, M.; Jeong, J.; Lu, H.; Lee, T. K.; Eickemeyer, F. T.; Liu, Y.; Choi, I. W.; Choi, S. J.; Jo, Y.; Kim, H.-B.; Mo, S.-I.; Kim, Y.-K.; Lee, H.; An, N. G.; Cho, S.; Tress, W. R.; Zakeeruddin, S. M.; Hagfeldt, A.; Kim, J. Y.; Grätzel, M.; Kim, D. S. Conformal Quantum Dot−SnO_2 Layers as Electron Transporters for Efficient Perovskite Solar Cells. *Science* **2022**, *375*, 302−306.

(5) Jung, E. H.; Jeon, N. J.; Park, E. Y.; Moon, C. S.; Shin, T. J.; Yang, T.-Y.; Noh, J. H.; Seo, J. Efficient, Stable and Scalable Perovskite Solar Cells Using Poly(3-Hexylthiophene. *Nature* **2019**, *567*, 511−515.

(6) Ashina, A.; Battula, R. K.; Ramasamy, E.; Chundi, N.; Sakthivel, S.; Veerappan, G. Dip Coated SnO_2 Film as Electron Transport Layer for Low Temperature Processed Planar Perovskite Solar Cells. *Appl. Surf. Sci. Adv.* **2021**, *4*, No. 100066.

(7) Raifuku, I.; Ishikawa, Y.; Chiang, Y.-H.; Lin, P.-Y.; Li, M.-H.; Uraoka, Y.; Chen, P. Segregation-Free Bromine-Doped Perovskite Solar Cells for IoT Applications. *RSC Adv.* **2019**, *9*, 32833−32838.

(8) Boix, P. P.; Nonomura, K.; Mathews, N.; Mhaisalkar, S. G. Current Progress and Future Perspectives for Organic/Inorganic Perovskite Solar Cells. *Mater. Today* **2014**, *17*, 16−23.

(9) Chu, Q.-Q.; Ding, B.; Peng, J.; Shen, H.; Li, X.; Liu, Y.; Li, C.-X.; Li, C.-J.; Yang, G.-J.; White, T. P.; Catchpole, K. R. Highly Stable Carbon-Based Perovskite Solar Cell with a Record Efficiency of over 18% via Hole Transport Engineering. *J. Mater. Sci. Technol.* **2019**, *35*, 987−993.

(10) Mohanraj, J.; Singh, C. R.; Gujar, T. P.; Heinrich, C. D.; Thelakkat, M. Nanostructured Hybrid Metal Mesh as Transparent Conducting Electrodes: Selection Criteria Verification in Perovskite Solar Cells. *Nanomaterials* **2021**, *11*, No. 1783.

(11) Ren, G.; Han, W.; Deng, Y.; Wu, W.; Li, Z.; Guo, J.; Bao, H.; Liu, C.; Guo, W. Strategies of Modifying Spiro-OMeTAD Materials

for Perovskite Solar Cells: A Review. *J. Mater. Chem. A* **2021**, *9*, 4589−4625.
(12) Tzounis, L.; Stergiopoulos, T.; Zachariadis, A.; Gravalidis, C.; Laskarakis, A.; Logothetidis, S. Perovskite Solar Cells from Small Scale Spin Coating Process towards Roll-to-Roll Printing: Optical and Morphological Studies. *Mater. Today: Proc.* **2017**, *4*, 5082−5089.
(13) Li, L.; Shen, W.; Yang, C.; Dou, Y.; Zhu, X.; Dong, Y.; Zhao, J.; Xiao, J.; Huang, F.; Cheng, Y.-B.; Zhong, J. In-Situ Monitored Chemical Bath Deposition of Planar NiO_x Layer for Inverted Perovskite Solar Cell with Enhanced Efficiency. *J. Mater. Sci. Technol.* **2023**, *133*, 145−153.
(14) Whitaker, J. B.; Kim, D. H.; Larson, B. W.; Zhang, F.; Berry, J. J.; van Hest, M. F. A. M.; Zhu, K. Scalable Slot-Die Coating of High Performance Perovskite Solar Cells. *Sustainable Energy Fuels* **2018**, *2*, 2442−2449.
(15) Bu, T.; Li, J.; Zheng, F.; Chen, W.; Wen, X.; Ku, Z.; Peng, Y.; Zhong, J.; Cheng, Y.-B.; Huang, F. Universal Passivation Strategy to Slot-Die Printed SnO_2 for Hysteresis-Free Efficient Flexible Perovskite Solar Module. *Nat. Commun.* **2018**, *9*, No. 4609.
(16) Chandrasekhar, P. S.; Chapagain, S.; Blake, M.; Armstrong, P. J.; Grapperhaus, C.; Druffel, T. L. Rapid Scalable Fabrication of Roll-to-Roll Slot-Die Coated Flexible Perovskite Solar Cells Using Intense Pulse Light Annealing. *Sustainable Energy Fuels* **2022**, *6*, 5316−5323.
(17) Peiris, T. A. N.; Benitez, J.; Sutherland, L.; Sharma, M.; Michalska, M.; Scully, A. D.; Vak, D.; Gao, M.; Weerasinghe, H. C.; Jasieniak, J. A Stable Aqueous SnO_2 Nanoparticle Dispersion for Roll-to-Roll Fabrication of Flexible Perovskite Solar Cells. *Coatings* **2022**, *12*, No. 1948.
(18) Hu, Y.; Niu, T.; Liu, Y.; Zhou, Y.; Xia, Y.; Ran, C.; Wu, Z.; Song, L.; Müller-Buschbaum, P.; Chen, Y.; Huang, W. Flexible Perovskite Solar Cells with High Power-Per-Weight: Progress, Application, and Perspectives. *ACS Energy Lett.* **2021**, *6*, 2917−2943.
(19) Howard, I. A.; Abzieher, T.; Hossain, I. M.; Eggers, H.; Schackmar, F.; Ternes, S.; Richards, B. S.; Lemmer, U.; Paetzold, U. W. Coated and Printed Perovskites for Photovoltaic Applications. *Adv. Mater.* **2019**, *31*, No. 1806702.
(20) Li, Z.; Wang, Z.; Jia, C.; Wan, Z.; Zhi, C.; Li, C.; Zhang, M.; Zhang, C.; Li, Z. Annealing Free Tin Oxide Electron Transport Layers for Flexible Perovskite Solar Cells. *Nano Energy* **2022**, *94*, No. 106919.
(21) Tang, G.; Yan, F. Recent Progress of Flexible Perovskite Solar Cells. *Nano Today* **2021**, *39*, No. 101155.
(22) Zhu, N.; Qi, X.; Zhang, Y.; Liu, G.; Wu, C.; Wang, D.; Guo, X.; Luo, W.; Li, X.; Hu, H.; Chen, Z.; Xiao, L.; Qu, B. High Efficiency (18.53%) of Flexible Perovskite Solar Cells via the Insertion of Potassium Chloride between SnO_2 and $CH_3NH_3PbI_3$ Layers. *ACS Appl. Energy Mater.* **2019**, *2*, 3676−3682.
(23) Rieu, M.; Camara, M.; Tournier, G.; Viricelle, J.-P.; Pijolat, C.; de Rooij, N. F.; Briand, D. Fully Inkjet Printed SnO_2 Gas Sensor on Plastic Substrate. *Sens. Actuators, B* **2016**, *236*, 1091−1097.
(24) Dong, J.; Jia, J.; Feng, X.; Shi, B.; Wu, Y.; Zhang, Y.; Wu, J.; Cao, B. Ligand Exchange of SnO_2 Effectively Improving the Efficiency of Flexible Perovskite Solar Cells. *J. Alloys Compd.* **2021**, *883*, No. 160827.
(25) Paik, M. J.; Yoo, J. W.; Park, J.; Noh, E.; Kim, H.; Ji, S.-G.; Kim, Y. Y.; Seok, S. I. SnO_2−TiO_2 Hybrid Electron Transport Layer for Efficient and Flexible Perovskite Solar Cells. *ACS Energy Lett.* **2022**, *7*, 1864−1870.
(26) Rohnacher, V.; Ullrich, F.; Eggers, H.; Schackmar, F.; Hell, S.; Salazar, A.; Huck, C.; Hernandez-Sosa, G.; Paetzold, U. W.; Jaegermann, W.; Pucci, A. Analytical Study of Solution-Processed Tin Oxide as Electron Transport Layer in Printed Perovskite Solar Cells. *Adv. Mater. Technol.* **2021**, *6*, No. 2000282.
(27) Zhuang, J.; Mao, P.; Luan, Y.; Chen, N.; Cao, X.; Niu, G.; Jia, F.; Wang, F.; Cao, S.; Wang, J. Rubidium Fluoride Modified SnO_2 for Planar n-i-p Perovskite Solar Cells. *Adv. Funct. Mater.* **2021**, *31*, No. 2010385.
(28) Tiwana, P.; Docampo, P.; Johnston, M. B.; Snaith, H. J.; Herz, L. M. Electron Mobility and Injection Dynamics in Mesoporous ZnO, SnO_2, and TiO_2 Films Used in Dye-Sensitized Solar Cells. *ACS Nano* **2011**, *5*, 5158−5166.
(29) Huang, L.; Sun, X.; Li, C.; Xu, J.; Xu, R.; Du, Y.; Ni, J.; Cai, H.; Li, J.; Hu, Z.; Zhang, J. UV-Sintered Low-Temperature Solution-Processed SnO_2 as Robust Electron Transport Layer for Efficient Planar Heterojunction Perovskite Solar Cells. *ACS Appl. Mater. Interfaces* **2017**, *9*, 21909−21920.
(30) Bahadur, J.; Ghahremani, A. H.; Martin, B.; Druffel, T.; Sunkara, M. K.; Pal, K. Solution Processed Mo Doped SnO_2 as an Effective ETL in the Fabrication of Low Temperature Planer Perovskite Solar Cell under Ambient Conditions. *Org. Electron.* **2019**, *67*, 159−167.
(31) Uddin, A.; Yi, H. Progress and Challenges of SnO_2 Electron Transport Layer for Perovskite Solar Cells: A Critical Review. *Sol. RRL* **2022**, *6*, No. 2100983.
(32) Altinkaya, C.; Aydin, E.; Ugur, E.; Isikgor, F. H.; Subbiah, A. S.; De Bastiani, M.; Liu, J.; Babayigit, A.; Allen, T. G.; Laquai, F.; Yildiz, A.; De Wolf, S. Tin Oxide Electron-Selective Layers for Efficient, Stable, and Scalable Perovskite Solar Cells. *Adv. Mater.* **2021**, *33*, No. 2005504.
(33) Kiani, M. S.; Sadirkhanov, Z. T.; Kakimov, A. G.; Parkhomenko, H. P.; Ng, A.; Jumabekov, A. N. Solution-Processed SnO_2 Quantum Dots for the Electron Transport Layer of Flexible and Printed Perovskite Solar Cells. *Nanomaterials* **2022**, *12*, No. 2615.
(34) Peiris, T. A. N.; Weerasinghe, H. C.; Sharma, M.; Kim, J.-E.; Michalska, M.; Chandrasekaran, N.; Senevirathna, D. C.; Li, H.; Chesman, A. S. R.; Vak, D.; Jasieniak, J. J. Non-Aqueous One-Pot SnO_2 Nanoparticle Inks and Their Use in Printable Perovskite Solar Cells. *Chem. Mater.* **2022**, *34*, 5535−5545.
(35) Shalenov, E. O.; Dzhumagulova, K. N.; Seitkozhanov, Y. S.; Ng, A.; Valagiannopoulos, C.; Jumabekov, A. N. Insights on Desired Fabrication Factors from Modeling Sandwich and Quasi-Interdigitated Back-Contact Perovskite Solar Cells. *ACS Appl. Energy Mater.* **2021**, *4*, 1093−1107.
(36) Zhang, X.; Qiu, J.; Li, X.; Zhao, J.; Liu, L. Complex Refractive Indices Measurements of Polymers in Visible and Near-Infrared Bands. *Appl. Opt.* **2020**, *59*, 2337−2344.
(37) Shalenov, E. O.; Seitkozhanov, Y. S.; Valagiannopoulos, C.; Ng, A.; Dzhumagulova, K. N.; Jumabekov, A. N. Performance Evaluation of Different Designs of Back-Contact Perovskite Solar Cells. *Sol. Energy Mater. Sol. Cells* **2022**, *234*, No. 111426.
(38) Parkhomenko, H. P.; Shalenov, E. O.; Umatova, Z.; Dzhumagulova, K. N.; Jumabekov, A. N. Fabrication of Flexible Quasi-Interdigitated Back-Contact Perovskite Solar Cells. *Energies* **2022**, *15*, No. 3056.
(39) Chander, S.; Purohit, A.; Nehra, A.; Nehra, S. P.; Dhaka, M. S. A Study on Spectral Response and External Quantum Efficiency of Mono-Crystalline Silicon Solar Cell. *Int. J. Renewable Energy Res.* **2015**, *5* 41−44. https://dergipark.org.tr/en/pub/ijrer/issue/16072/167986.
(40) Slami, A.; Benramdane, N. Manual Method for Measuring the External Quantum Efficiency for Solar Cells. *E3S Web Conf.* **2021**, *229*, No. 01005.
(41) Laquai, F.; Andrienko, D.; Deibel, C.; Neher, D. Charge Carrier Generation, Recombination, and Extraction in Polymer−Fullerene Bulk Heterojunction Organic Solar Cells. In *Elementary Processes in Organic Photovoltaics*; Springer: Cham, pp 267−291.
(42) Karki, A.; Vollbrecht, J.; Gillett, A. J.; Selter, P.; Lee, J.; Peng, Z.; Schopp, N.; Dixon, A. L.; Schrock, M.; Nádaždy, V.; Schauer, F.; Ade, H.; Chmelka, B. F.; Bazan, G. C.; Friend, R. H.; Nguyen, T.-Q. Unifying Charge Generation, Recombination, and Extraction in Low-Offset Non-Fullerene Acceptor Organic Solar Cells. *Adv. Energy Mater.* **2020**, *10*, No. 2001203.
(43) Sze, S. M.; Li, Y.; Ng, K. K. *Physics of Semiconductor Devices*; John Wiley & Sons, 2021.
(44) Wagner, L.; Schygulla, P.; Herterich, J. P.; Elshamy, M.; Bogachuk, D.; Zouhair, S.; Mastroianni, S.; Würfel, U.; Liu, Y.; Zakeeruddin, S. M.; Grätzel, M.; Hinsch, A.; Glunz, S. W. Revealing Fundamentals of Charge Extraction in Photovoltaic Devices through

https://doi.org/10.1021/acsomega.3c02341
ACS Omega 2023, 8, 21212−21222

Potentiostatic Photoluminescence Imaging. *Matter* **2022**, *5*, 2352−2364.
(45) Le Corre, V. M.; Duijnstee, E. A.; El Tambouli, O.; Ball, J. M.; Snaith, H. J.; Lim, J.; Koster, L. J. A. Revealing Charge Carrier Mobility and Defect Densities in Metal Halide Perovskites via Space-Charge-Limited Current Measurements. *ACS Energy Lett.* **2021**, *6*, 1087−1094.
(46) Han, X.; Wang, X.; Feng, J.; Huang, H.; Zhu, Z.; Yu, T.; Li, Z.; Zou, Z. Carrier Mobility Enhancement in (121)-Oriented $CsPbBr_3$ Perovskite Films Induced by the Microstructure Tailoring of $PbBr_2$ Precursor Films. *ACS Appl. Electron. Mater.* **2021**, *3*, 373−384.
(47) Yang, D.; Yang, R.; Ren, X.; Zhu, X.; Yang, Z.; Li, C.; Liu, S. Hysteresis-Suppressed High-Efficiency Flexible Perovskite Solar Cells Using Solid-State Ionic-Liquids for Effective Electron Transport. *Adv. Mater.* **2016**, *28*, 5206−5213.
(48) Poglitsch, A.; Weber, D. Dynamic Disorder in Methylammoniumtrihalogenoplumbates (II) Observed by Millimeter-wave Spectroscopy. *J. Chem. Phys.* **1987**, *87*, 6373−6378.
(49) Feng, Y.; Liu, R.; Li, F.; Jin, M.; Du, Q.; Rong, Y.; Hu, H.; Wang, M.; Li, Y.; Shen, Z.; Liu, Y.; Li, H.; Chen, C. A Synergistic Co-Passivation Strategy for High-Performance Perovskite Solar Cells with Large Open Circuit Voltage. *J. Mater. Chem. C* **2022**, *10*, 12699−12707.
(50) Guo, R.; Bao, C.; Gao, F.; Tian, J. Double Active Layers Constructed with Halide Perovskite and Quantum Dots for Broadband Photodetection. *Adv. Opt. Mater.* **2020**, *8*, No. 2000557.
(51) Jia, P.; Qin, L.; Zhao, D.; Tang, Y.; Song, B.; Guo, J.; Li, X.; Li, L.; Cui, Q.; Hu, Y.; Lou, Z.; Teng, F.; Hou, Y. The Trapped Charges at Grain Boundaries in Perovskite Solar Cells. *Adv. Funct. Mater.* **2021**, *31*, No. 2107125.
(52) Brus, V. V.; Schopp, N.; Ko, S.-J.; Vollbrecht, J.; Lee, J.; Karki, A.; Bazan, G. C.; Nguyen, T.-Q. Temperature and Light Modulated Open-Circuit Voltage in Nonfullerene Organic Solar Cells with Different Effective Bandgaps. *Adv. Energy Mater.* **2021**, *11*, No. 2003091.
(53) Tress, W.; Yavari, M.; Domanski, K.; Yadav, P.; Niesen, B.; Baena, J. P. C.; Hagfeldt, A.; Graetzel, M. Interpretation and Evolution of Open-Circuit Voltage, Recombination, Ideality Factor and Subgap Defect States during Reversible Light-Soaking and Irreversible Degradation of Perovskite Solar Cells. *Energy Environ. Sci.* **2018**, *11*, 151−165.
(54) Brus, V. V.; Proctor, C. M.; Ran, N. A.; Nguyen, T.-Q. Capacitance Spectroscopy for Quantifying Recombination Losses in Nonfullerene Small-Molecule Bulk Heterojunction Solar Cells. *Adv. Energy Mater.* **2016**, *6*, No. 1502250.
(55) Kirchartz, T.; Deledalle, F.; Tuladhar, P. S.; Durrant, J. R.; Nelson, J. On the Differences between Dark and Light Ideality Factor in Polymer:Fullerene Solar Cells. *J. Phys. Chem. Lett.* **2013**, *4*, 2371−2376.
(56) Fahrenbruch, A.; Bube, R. *Fundamentals of Solar Cells: Photovoltaic Solar Energy Conversion*; Elsevier, 2012.
(57) Kirchartz, T.; Nelson, J. Meaning of Reaction Orders in Polymer:Fullerene Solar Cells. *Phys. Rev. B* **2012**, *86*, No. 165201.
(58) Lei, Y.; Xu, Y.; Wang, M.; Zhu, G.; Jin, Z. Origin, Influence, and Countermeasures of Defects in Perovskite Solar Cells. *Small* **2021**, *17*, No. 2005495.
(59) Ball, J. M.; Petrozza, A. Defects in Perovskite-Halides and Their Effects in Solar Cells. *Nat. Energy* **2016**, *1*, No. 16149.
(60) Brus, V. V. Light Dependent Open-Circuit Voltage of Organic Bulk Heterojunction Solar Cells in the Presence of Surface Recombination. *Org. Electron.* **2016**, *29*, 1−6.
(61) Vollbrecht, J.; Brus, V. V. On the Recombination Order of Surface Recombination under Open Circuit Conditions. *Org. Electron.* **2020**, *86*, No. 105905.
(62) Ren, Z.; Liu, K.; Hu, H.; Guo, X.; Gao, Y.; Fong, P. W. K.; Liang, Q.; Tang, H.; Huang, J.; Zhang, H.; Qin, M.; Cui, L.; Chandran, H. T.; Shen, D.; Lo, M.-F.; Ng, A.; Surya, C.; Shao, M.; Lee, C.-S.; Lu, X.; Laquai, F.; Zhu, Y.; Li, G. Room-Temperature Multiple Ligands-Tailored SnO_2 Quantum Dots Endow in Situ Dual-Interface Binding for Upscaling Efficient Perovskite Photovoltaics with High V_{OC}. *Light Sci. Appl.* **2021**, *10*, No. 239.
(63) Noh, M. F. M.; Arzaee, N. A.; Safaei, J.; Mohamed, N. A.; Kim, H. P.; Yusoff, A. R. M.; Jang, J.; Teridi, M. A. M. Eliminating Oxygen Vacancies in SnO_2 Films via Aerosol-Assisted Chemical Vapour Deposition for Perovskite Solar Cells and Photoelectrochemical Cells. *J. Alloys Compd.* **2019**, *773*, 997−1008.
(64) Zhang, F.; Ma, W.; Guo, H.; Zhao, Y.; Shan, X.; Jin, K.; Tian, H.; Zhao, Q.; Yu, D.; Lu, X.; Lu, G.; Meng, S. Interfacial Oxygen Vacancies as a Potential Cause of Hysteresis in Perovskite Solar Cells. *Chem. Mater.* **2016**, *28*, 802−812.
(65) Abdi-Jalebi, M.; Andaji-Garmaroudi, Z.; Cacovich, S.; Stavrakas, C.; Philippe, B.; Richter, J. M.; Alsari, M.; Booker, E. P.; Hutter, E. M.; Pearson, A. J.; Lilliu, S.; Savenije, T. J.; Rensmo, H.; Divitini, G.; Ducati, C.; Friend, R. H.; Stranks, S. D. Maximizing and Stabilizing Luminescence from Halide Perovskites with Potassium Passivation. *Nature* **2018**, *555*, 497−501.
(66) Yang, J.-N.; Song, Y.; Yao, J.-S.; Wang, K.-H.; Wang, J.-J.; Zhu, B.-S.; Yao, M.-M.; Rahman, S. U.; Lan, Y.-F.; Fan, F.-J.; Yao, H.-B. Potassium Bromide Surface Passivation on $CsPbI_3$-XBr_x Nanocrystals for Efficient and Stable Pure Red Perovskite Light-Emitting Diodes. *J. Am. Chem. Soc.* **2020**, *142*, 2956−2967.
(67) Abdi-Jalebi, M.; Andaji-Garmaroudi, Z.; Pearson, A. J.; Divitini, G.; Cacovich, S.; Philippe, B.; Rensmo, H.; Ducati, C.; Friend, R. H.; Stranks, S. D. Potassium- and Rubidium-Passivated Alloyed Perovskite Films: Optoelectronic Properties and Moisture Stability. *ACS Energy Lett.* **2018**, *3*, 2671−2678.
(68) Kim, B. J.; Kim, D. H.; Lee, Y.-Y.; Shin, H.-W.; Han, G. S.; Hong, J. S.; Mahmood, K.; Ahn, T. K.; Joo, Y.-C.; Hong, K. S.; Park, N.-G.; Lee, S.; Jung, H. S. Highly Efficient and Bending Durable Perovskite Solar Cells: Toward a Wearable Power Source. *Energy Environ. Sci.* **2015**, *8*, 916−921.
(69) Heo, J. H.; Shin, D. H.; Jang, M. H.; Lee, M. L.; Kang, M. G.; Im, S. H. Highly Flexible, High-Performance Perovskite Solar Cells with Adhesion Promoted $AuCl_3$-Doped Graphene Electrodes. *J. Mater. Chem. A* **2017**, *5*, 21146−21152.
(70) Popoola, I. K.; Gondal, M. A.; Qahtan, T. F. Recent Progress in Flexible Perovskite Solar Cells: Materials, Mechanical Tolerance and Stability. *Renewable Sustainable Energy Rev.* **2018**, *82*, 3127−3151.
(71) Sears, K. K.; Fievez, M.; Gao, M.; Weerasinghe, H. C.; Easton, C. D.; Vak, D. ITO-Free Flexible Perovskite Solar Cells Based on Roll-to-Roll, Slot-Die Coated Silver Nanowire Electrodes. *Sol. RRL* **2017**, *1*, No. 1700059.
(72) Dong, Q.; Chen, M.; Liu, Y.; Eickemeyer, F. T.; Zhao, W.; Dai, Z.; Yin, Y.; Jiang, C.; Feng, J.; Jin, S.; Liu, S. F.; Zakeeruddin, S. M.; Grätzel, M.; Padture, N. P.; Shi, Y. Flexible Perovskite Solar Cells with Simultaneously Improved Efficiency, Operational Stability, and Mechanical Reliability. *Joule* **2021**, *5*, 1587−1601.
(73) Li, M.; Yang, Y.-G.; Wang, Z.-K.; Kang, T.; Wang, Q.; Turren-Cruz, S.-H.; Gao, X.-Y.; Hsu, C.-S.; Liao, L.-S.; Abate, A. Perovskite Grains Embraced in a Soft Fullerene Network Make Highly Efficient Flexible Solar Cells with Superior Mechanical Stability. *Adv. Mater.* **2019**, *31*, No. 1901519.
(74) Jiang, N.-R.; Wang, Y.-F.; Dong, Q.-F.; Ge, C.-D.; Yang, Z.-Q.; Yin, D.; Liu, Y.-F.; Bi, Y.-G.; Feng, J.; Sun, H.-B. Enhanced Efficiency and Mechanical Robustness of Flexible Perovskite Solar Cells by Using $HPbI_3$ Additive. *Sol. RRL* **2021**, *5*, No. 2000821.

https://doi.org/10.1021/acsomega.3c02341
ACS Omega 2023, 8, 21212−21222